Volume 13
Number 13
7 April 2025
Pages 4033-4240

Journal of Materials Chemistry B

Materials for biology and medicine

rsc.li/materials-b

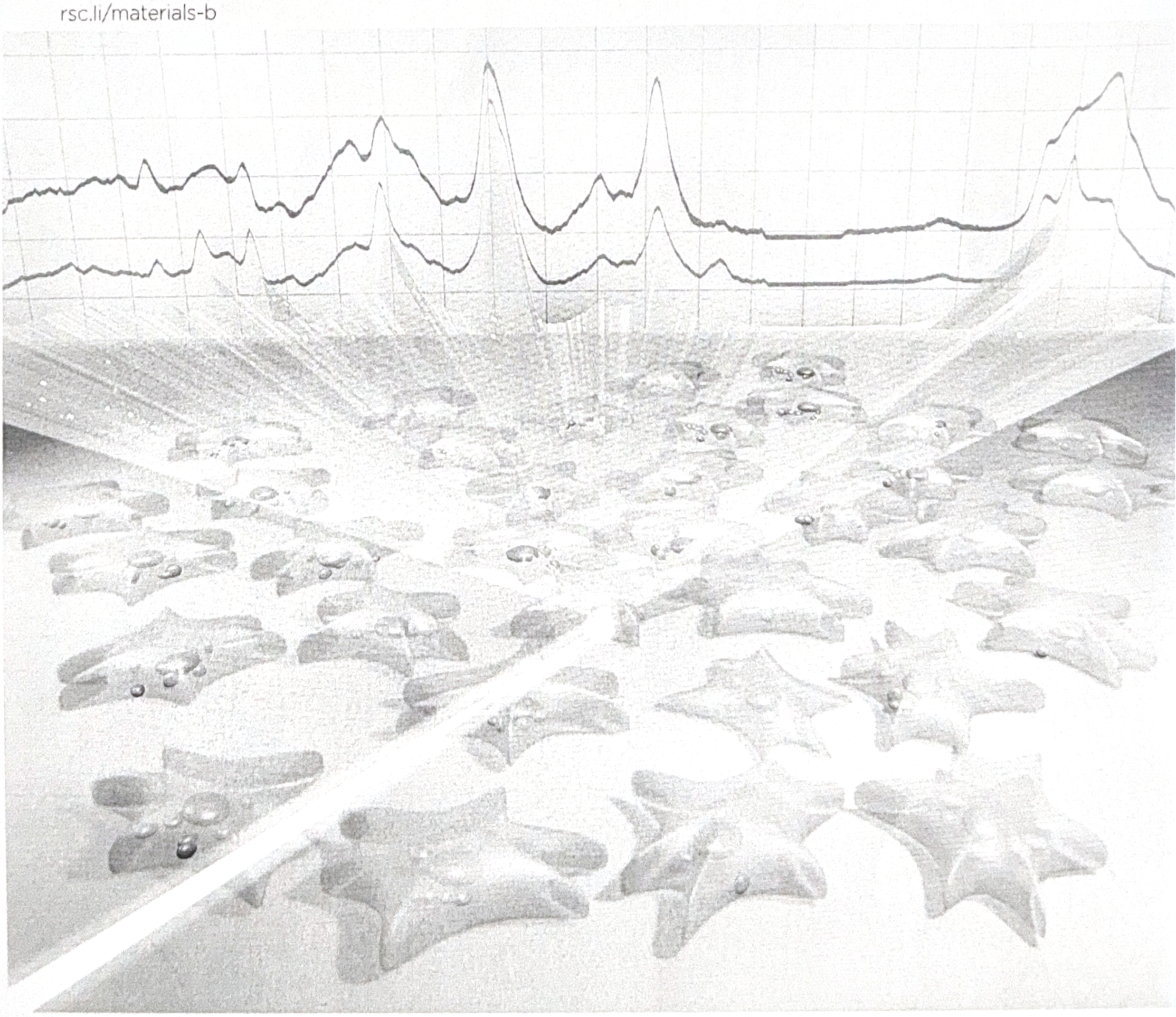

ISSN 2050-750X

ROYAL SOCIETY OF CHEMISTRY

PAPER
Patrizio Candeloro *et al.*
Raman imaging investigation of hepatic LX-2 cell reversion under different lipidic treatments

Environmental Science: Atmospheres

GOLD OPEN ACCESS

Connecting communities and inspiring new ideas

Journal of Materials Chemistry B

ROYAL SOCIETY OF CHEMISTRY

View Article Online
View Journal | View Issue

COMMUNICATION

Check for updates

Cite this: *J. Mater. Chem. B*, 2025, 13, 4073

Received 22nd January 2025,
Accepted 4th March 2025

DOI: 10.1039/d5tb00152h

rsc.li/materials-b

A PEGylated conjugated-BODIPY oligomer for NIR-II imaging-guided photothermal therapy†

Yuan Wang,‡ Tongtong Shan,‡ Jiahao Zheng, Jia Tian and Weian Zhang *

The integration of second near-infrared (NIR-II) fluorescence imaging and photothermal therapy (PTT) achieved precise and efficient tumor treatment. BODIPY, a promising fluorescent dye, is widely used in biological fluorescence imaging due to its excellent optical properties and chemical stability. However, the excitation wavelengths of BODIPY typically range from 530 nm to 650 nm within the visible spectrum, which significantly limits tissue penetration. In this work, a self-assembled nanoparticle ($BODIPY_4$–PEG NP) was fabricated with a BODIPY-conjugated oligomer ($BODIPY_4$) bearing a hydrophilic polyethylene glycol (PEG) chain. $BODIPY_4$–PEG NPs exhibit excellent NIR-II emission, with a maximum fluorescence emission peak of 1123 nm. The outstanding imaging performance of $BODIPY_4$–PEG NPs has been evaluated in the imaging of lymph nodes and the vascular system in mice, demonstrating excellent spatial resolution. Based on the excellent imaging performance and photothermal conversion efficiency (35%) of the $BODIPY_4$–PEG NPs, they can be further utilized in NIR-II imaging-guided photothermal therapy. In a 4T1 tumor-bearing mouse model, $BODIPY_4$–PEG NPs exhibited strong fluorescence under 980 nm laser irradiation and successfully induced heat generation to eliminate the tumor. To summarize, $BODIPY_4$–PEG NPs contribute to the ongoing progress in the field of NIR-II fluorescence imaging-guided PTT.

Introduction

Photothermal therapy (PTT) is an attractive treatment that utilizes photothermal agents (PTAs) to generate heat under excitation light for tumor destruction, offering advantages such as high efficiency, non-invasiveness, minimal side effects, and non-resistance.[1–3] In recent decades, various PTAs have been explored for precise diagnosis and effective treatment of cancer,[4–8] such as noble metal,[9] metallic oxides,[10] and semiconducting polymers.[11] However, many PTAs can only be activated by visible light, which has poor tissue penetration capability.[12,13] Researchers have developed some novel NIR-II photosensitizers, such as cyanine-based dyes,[14] quantum dots,[15] and polymer-based systems.[16] These photosensitizers exhibit better tissue penetration in the NIR-II region. However, these materials often face challenges such as poor photostability, fluorescence quenching caused by aggregation, and low photothermal conversion efficiency.[17] An urgent need exists for PTAs that possess excellent photostability and high photothermal conversion efficiency (PCE) to enable efficient PTT.[18] The precision of treatment can be enhanced and the effectiveness of photothermal therapy optimized through fluorescence-imaging guidance.[19–21] NIR-II imaging offers better tissue penetration and reduced light scattering, making it suitable for deep-tissue imaging and providing clear imaging at greater tissue depths.[13,22] Therefore, the development of PTAs with NIR-II emission is crucial for advancing fluorescence imaging-guided precision PTT.[23,24]

BODIPY is an organic PTA characterized by its easy functionalization, outstanding photostability, and high PCE.[20,25] It is commonly employed in the field of photothermal diagnosis and therapy. However, the maximum absorption peak of conventional BODIPY falls within the visible region, which limits its tissue penetration capability.[26,27] Researchers have red-shifted the absorption wavelength of BODIPY to the near-infrared region by introducing conjugated groups[28] and using metal coordination methods.[29] However, the introduction of conjugated groups may cause aggregation of the molecules, thereby reducing the efficiency of the photosensitizers. Additionally, the stability of metal-coordinated BODIPY may be affected by environmental factors, which could influence the photodynamic therapy (PDT) effect. Furthermore, the poor water solubility of BODIPY leads to significant aggregation in aqueous solutions.[30] Although these aggregates can induce a red shift in the absorption region, they also cause fluorescence quenching, preventing its use in fluorescence imaging.[31] To address this challenge, Badon *et al.*[32] synthesized a water-soluble PEGylated BODIPY derivative, which significantly

Shanghai Key Laboratory of Functional Materials Chemistry, East China University of Science and Technology, Shanghai 200237, China

† Electronic supplementary information (ESI) available. See DOI: https://doi.org/10.1039/d5tb00152h

‡ Yuan Wang and Tongtong Shan contributed equally to this work.

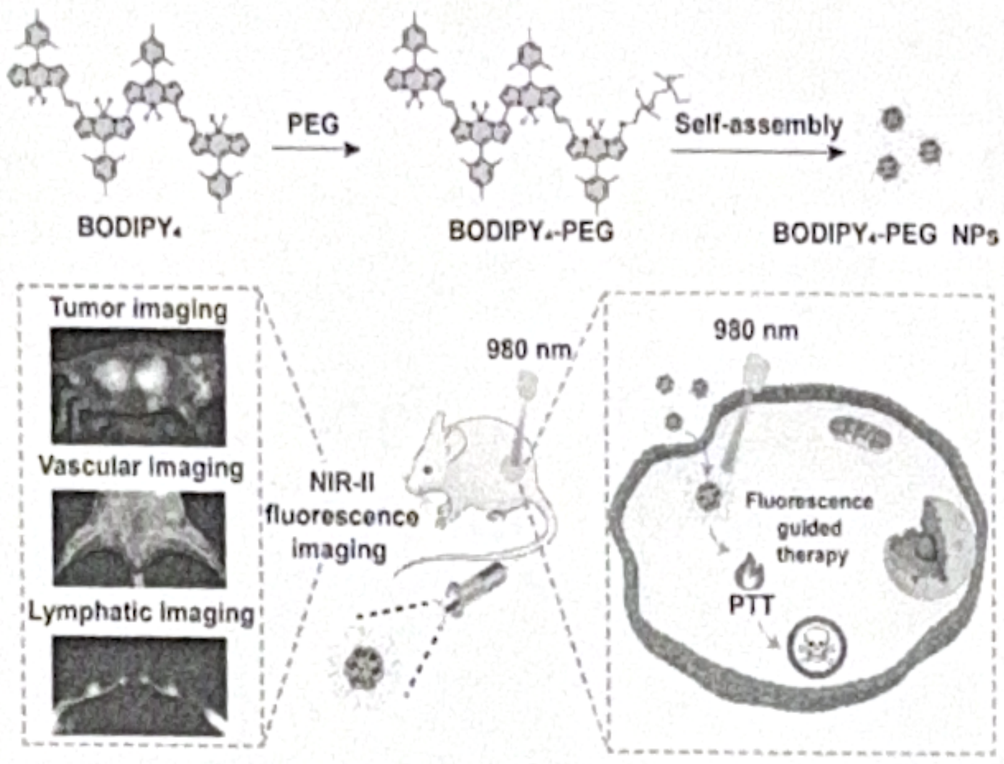

Scheme 1 Schematic illustration of $BODIPY_4$–PEG NPs for NIR-II fluorescence imaging guided PTT.

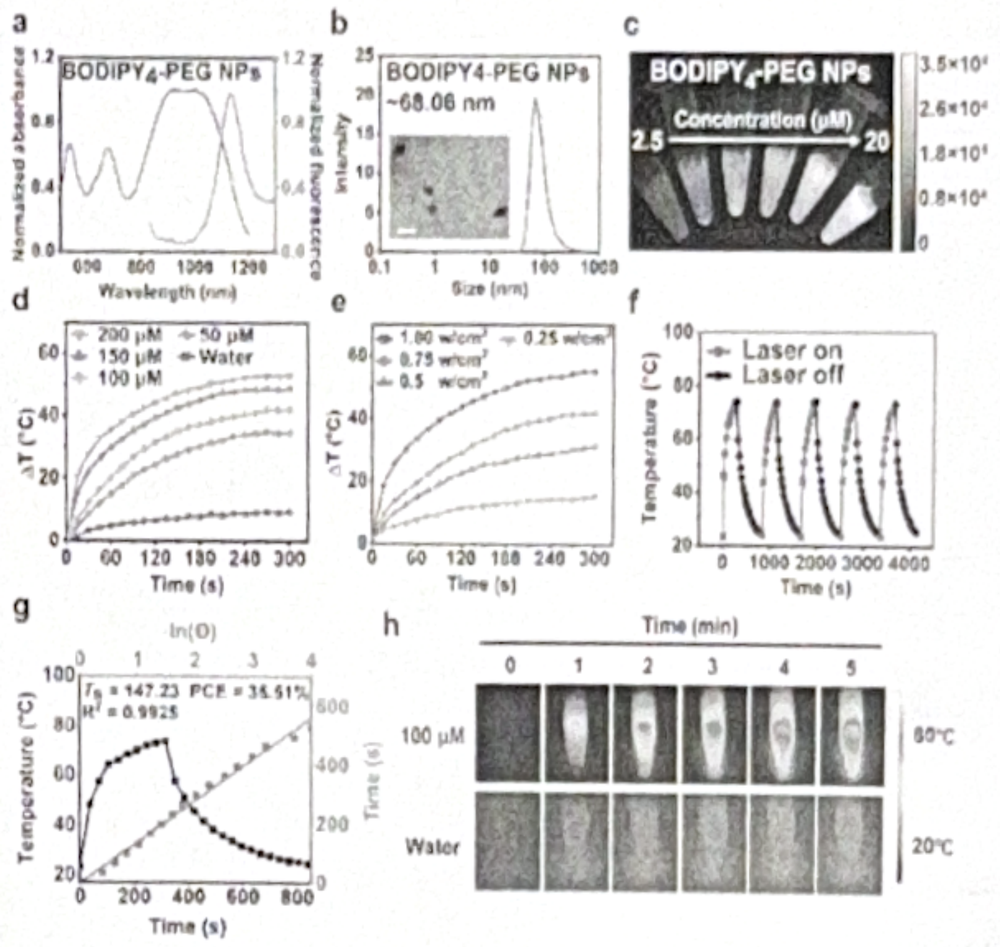

Fig. 1 (a) Absorption and fluorescence emission spectra of $BODIPY_4$–PEG NPs. (b) DLS and TEM characterizations for $BODIPY_4$–PEG NPs in aqueous solution. (c) Fluorescence image at different concentrations of $BODIPY_4$–PEG NPs. Photothermal conversion curves of $BODIPY_4$–PEG NP aqueous solution at (d) various concentrations and (e) power densities under 980 nm laser irradiation for 5 min (the concentration of $BODIPY_4$–PEG NPs was kept at 100 μM). (f) Photothermal stability of $BODIPY_4$–PEG NPs. The heating and cooling cyclic curves of $BODIPY_4$–PEG NPs (100 μM) under 980 nm laser irradiation (1.00 W cm^{-2}, 5 cycles). (g) The heating–cooling curve of $BODIPY_4$–PEG NP aqueous solution (100 μM) under 980 nm laser irradiation (1.00 W cm^{-2}) (heating time 5 min, cooling time 9 min) and the relationship between $-\ln(\theta)$ and cooling time calculated by the curve and formula. (h) Thermal images of $BODIPY_4$–PEG NPs and water under 980 nm laser irradiation (1.00 W cm^{-2}, 5 min).

improved the water solubility of BODIPY. Unfortunately, this approach did not achieve efficient fluorescence emission in the NIR-II region. Therefore, optimizing the structure of BODIPY to achieve efficient NIR-II fluorescence imaging-guided PTT is still a key challenge that needs further exploration.

Herein, we designed and synthesized a BODIPY oligomer ($BODIPY_4$), which was then modified with polyethylene glycol (PEG) to obtain amphiphilic $BODIPY_4$–PEG. This was further self-assembled in aqueous solution to construct $BODIPY_4$–PEG nanoparticles ($BODIPY_4$–PEG NPs). Polymer-based NIR-II photosensitizers often enhance stability and water solubility by encapsulating dyes or metal ion complexes with polymers.[33] However, these approaches may suffer from issues such as uneven surface functionalization, which can affect their stability and performance *in vivo*. In contrast, the stability of the nanoparticles could be enhanced by modifying $BODIPY_4$ with PEG to obtain amphiphilic $BODIPY_4$–PEG. $BODIPY_4$–PEG NPs exhibit strong fluorescence emission in the NIR-II region. The $BODIPY_4$–PEG NPs not only possess good water-solubility and biocompatibility, but also enable prolonged blood circulation, thereby allowing better modulation of drug dosage. The NIR-II imaging ability of $BODIPY_4$–PEG NPs was verified by *in vivo* vascular imaging, tumor imaging and lymphatic imaging. In addition, the photothermal effect was validated in a 4T1 tumor-bearing mouse model. Thus, the construction of a BODIPY-based oligomer enhances the water-soluble and fluorescence imaging performance of BODIPY, thereby optimizing its properties in the NIR-II region for better guidance of PTT (Scheme 1).

Results and discussion

Preparation and characterization

The synthesis and characterization of $BODIPY_4$ are detailed in the ESI† (Schemes S1–S5). The maximum absorption wavelength of $BODIPY_4$, composed of four conjugated BODIPY monomers, is at 955 nm (Fig. S1, ESI†). However, its fluorescence emission peak red shifts to 1015 nm within the NIR-II window, which is superior to the fluorescence emission reported for BODIPY dimers in previous literature.[34] However, extensively conjugated structures are usually associated with poor water solubility. To improve the water solubility of $BODIPY_4$, $BODIPY_4$–PEG was prepared by chemical modification with the PEG chain on $BODIPY_4$. The maximum absorption and fluorescence emission peaks of $BODIPY_4$–PEG NPs in aqueous solution were at 931 and 1123 nm, respectively (Fig. 1a). The absorption band covered the 800–1100 nm wavelength range. As presented in Fig. 1b, the $BODIPY_4$–PEG NPs in water showed an average hydrodynamic diameter of approximately 68.10 nm, with a polydispersity index (PDI) of 0.12, indicating a narrow size distribution. The good water solubility of $BODIPY_4$–PEG NPs favours the excellent photophysical properties. The fluorescence intensity of $BODIPY_4$–PEG NPs increased as the concentration increased (Fig. 1c and Fig. S2, ESI†). Furthermore, compared to the commercial NIR fluorescence probe ICG, $BODIPY_4$–PEG NPs exhibited outstanding photostability (Fig. S3, ESI†).

Due to the broad absorption peaks of $BODIPY_4$–PEG NPs, 808 nm, 980 nm and 1064 nm lasers were utilized to explore the *in vitro* photothermal properties of $BODIPY_4$–PEG NPs for their potential application in PTT (Fig. 1d–h and Fig. S4 and S5, ESI†). The temperature increases of $BODIPY_4$–PEG NPs showed a significant dependence on both concentration and laser intensity. After five heating and cooling cycles, $BODIPY_4$–PEG NPs exhibited outstanding photothermal stability under irradiation with 808 nm, 980 nm, and 1064 nm lasers. The photothermal

conversion efficiency (PCE) of $BODIPY_4$–PEG NPs under these three laser irradiations is summarized and compared in Fig. S6 (ESI†), and $BODIPY_4$–PEG NPs achieved the highest PCE (35.51%) under 980 nm laser irradiation.

In vitro assessments of cellular uptake and photothermal effect

Effective cellular uptake of PTAs is of great significance for cancer treatment.[35,36] Based on the good NIR-II imaging capability of $BODIPY_4$–PEG NPs, different concentrations of $BODIPY_4$–PEG NPs were co-incubated with 4T1 and 3T3 cells for 12 h and 24 h to investigate the cellular uptake behavior by fluorescence imaging. As shown in Fig. 2a and Fig. S7 (ESI†), the fluorescence intensity increased gradually with the concentration of $BODIPY_4$–PEG NPs and cultivation time, indicating that $BODIPY_4$–PEG NPs could be effectively taken up by cells. Furthermore, a CCK-8 assay verified that $BODIPY_4$–PEG Ns exhibited no significant cytotoxicity after co-incubation with 4T1 cells at various concentrations (maximum 100 μM) for 24 h without laser irradiation (Fig. 2b). After continuous 980 nm laser irradiation for 5 min, the cell viability decreased significantly in a concentration-dependent manner, especially at the $BODIPY_4$–PEG NP concentration of 50 μM (Fig. 2c). Then, the phototoxicity of $BODIPY_4$–PEG NPs against 4T1 tumor cells was further evaluated by live/dead assay with calcein-acetoxymethyl ester (calcein-AM, living cells, green fluorescence) and propidium iodide (PI, dead cells, red fluorescence) staining. As exhibited in Fig. 2d, the $BODIPY_4$–PEG NPs with 980 nm laser irradiation ($BODIPY_4$–PEG NPs + L) group exhibited distinct red fluorescence, demonstrating the good photothermal effect of $BODIPY_4$–PEG NPs against tumor cells.

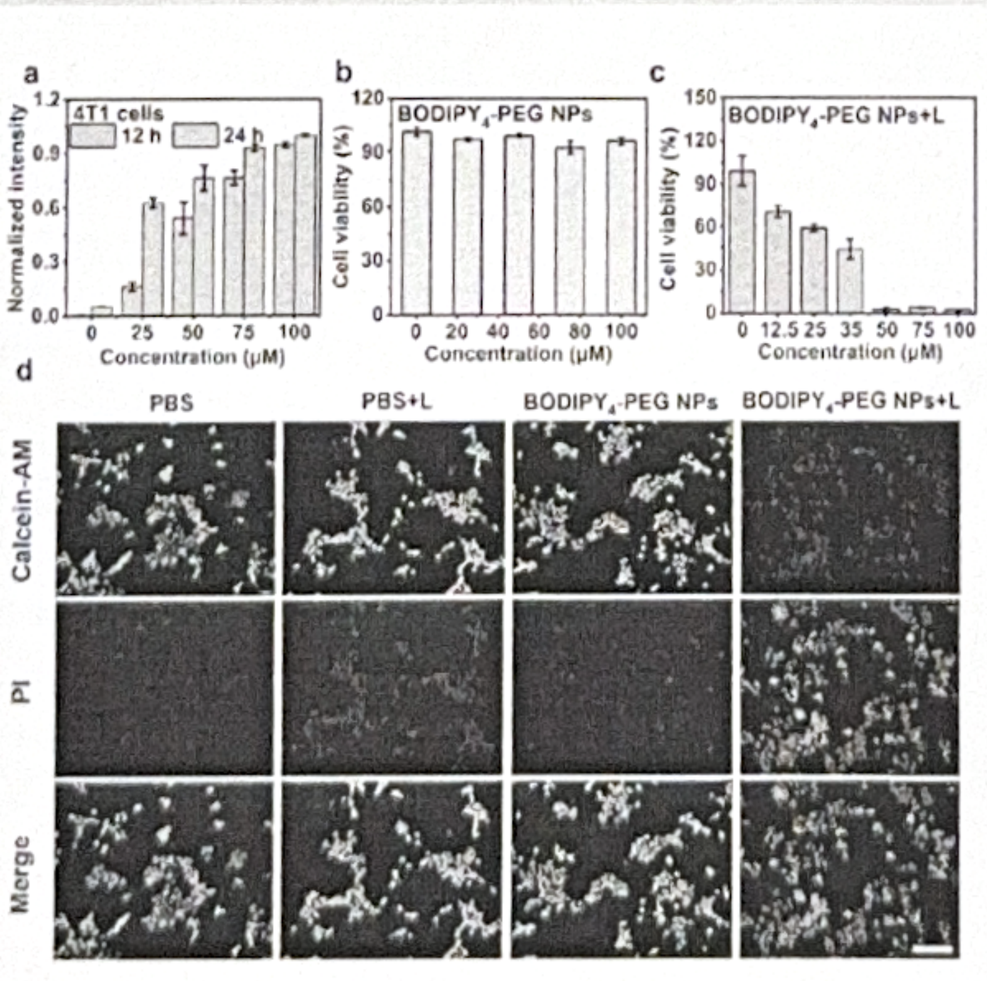

Fig. 2 (a) Quantitative statistic of cellular uptake intensity by 4T1 cells after the *co*-incubation with $BODIPY_4$–PEG NPs for 12 h or 24 h. (b) and (c) Cell viability of 4T1 cells incubated with $BODIPY_4$–PEG NPs at different concentrations without or with 980 nm laser exposure. (d) Live/dead assay of 4T1 cells stained with calcein-AM and PI treated with PBS, PBS + L, $BODIPY_4$–PEG NPs, and $BODIPY_4$–PEG NPs + L (50 μM). Scale bar: 500 μm. Data are presented as mean ± SEM (n = 3 per group), where n represents the number of independent experiments.

Meanwhile, the cells treated with PBS, PBS + L, and $BODIPY_4$–PEG NPs groups showed strong green fluorescence, revealing that neither $BODIPY_4$–PEG NPs alone nor 980 nm laser irradiation caused obvious damage to the cells.

In vivo NIR-II fluorescence imaging

Based on the strong fluorescence emission of $BODIPY_4$–PEG NPs at the NIR-II region, the *in vivo* fluorescence imaging experiment was first conducted to image the whole-body vasculature of mice. After tail vein injection of $BODIPY_4$–PEG NPs, the vasculature of the abdomen and hind limb was clearly distinguished from the surrounding tissues, with the signal-to-background (S/B) ratios reaching a maximum of 1.68 and 2.18, respectively (Fig. 3a–e). Additionally, the blood vessels on the back of a mouse were also clearly visualized (Fig. 3f). Subsequently, to label the lymph nodes and lymphatic vessels of mice, $BODIPY_4$–PEG NPs were injected into the rear paw. The mice were then imaged at different time points. The popliteal and sacral lymph nodes in the hind limb were gradually illuminated over time (Fig. 4a). As shown in Fig. 4b, the intensity of popliteal lymph node to normal tissue (LN/NT) ratios of $BODIPY_4$–PEG NPs increased to the maximum at 20–40 min post-injection. The S/B ratios of the popliteal lymph node to surrounding normal tissues reached a maximum of 13.79 at 40 min post-injection. Furthermore, benefiting from the high penetration depth of NIR-II fluorescence imaging, three major lymphatic vessels were monitored and their cross-sectional fluorescence intensity was analyzed (Fig. 4c and d).[37,38] In summary, $BODIPY_4$–PEG NPs have good fluorescence imaging ability in the NIR-II region and can be used to label lymph nodes and lymphatic vessels in mice, and the best imaging effect can be achieved within 20 to 40 min after surgery, showing potential biomedical applications.

Persistent angiogenesis plays a vital role in tumor growth and metastasis, and monitoring tumor angiogenesis can provide valuable insights into tumor progression.[38,39] After tail vein injection of $BODIPY_4$–PEG NPs into mice with subcutaneous 4T1 tumors implanted in the left thigh, the rich vascular system at the tumor site was monitored with the assistance of the NIR-II imaging system (Fig. 4e). This phenomenon can be attributed to

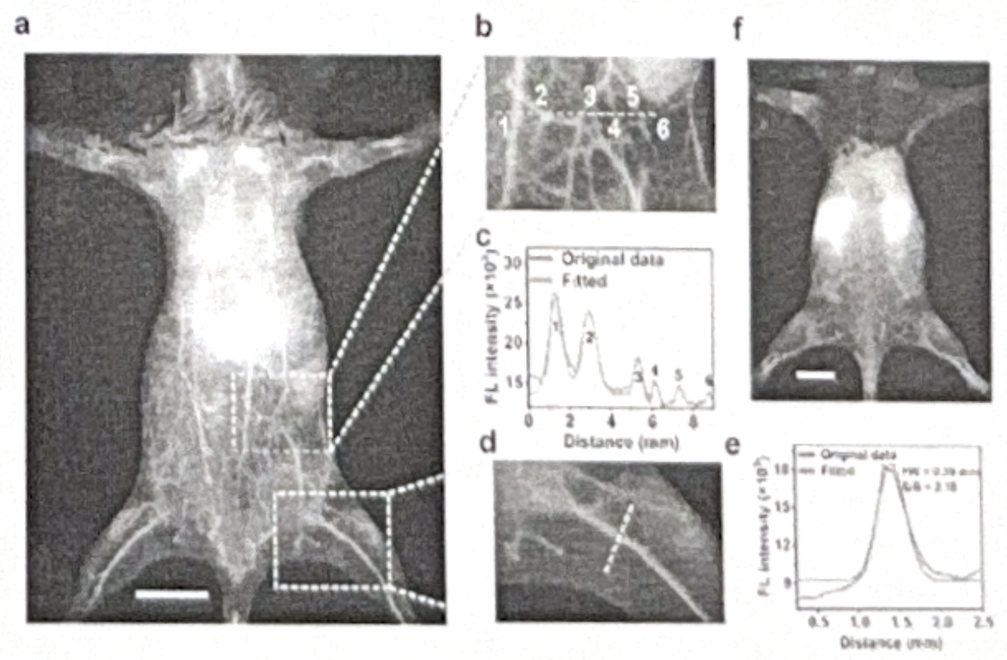

Fig. 3 (a) Abdominal angiography of mice. (b)–(e) Line intensities of the region of interest. (f) Back angiography. (1 mM, 50 μL, 980 nm, 1150 nm long pass filter, exposure time: 300 ms). Scale bar: 10 mm.

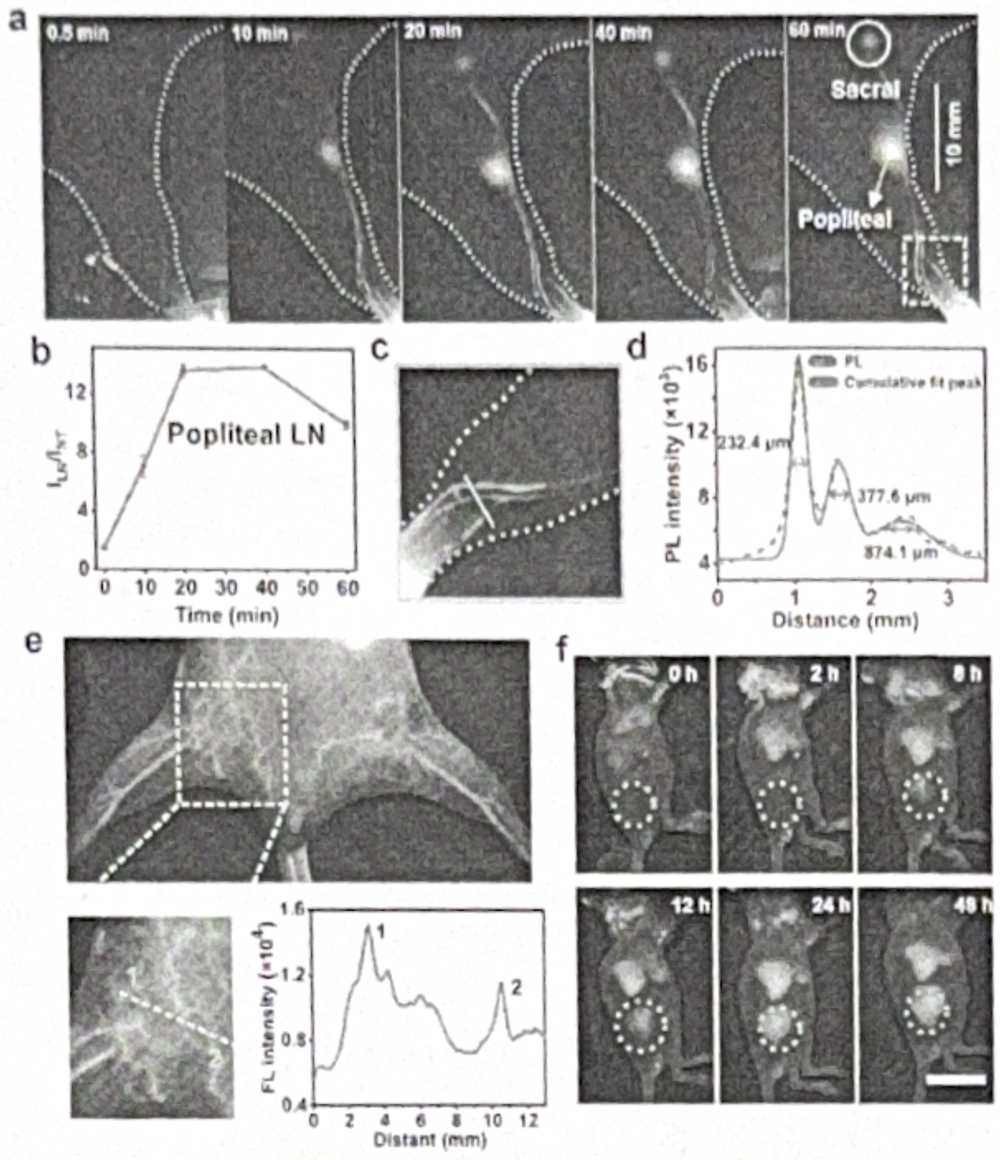

Fig. 4 (a) Fluorescence images of popliteal and sacral lymph nodes after footpad injection of $BODIPY_4$–PEG NPs (1 mM, 20 μL, 1150 nm LP) at different times. (b) Intensity of the popliteal lymph node to normal tissue (LN/NT) ratios of $BODIPY_4$–PEG NPs. (c) The locally enlarged picture of lymphatic vessels and (d) the cross-sectional intensity profile along the white line. (e) Vascular imaging of the orthotopic 4T1 tumor. (f) NIR-II fluorescence imaging of $BODIPY_4$–PEG NPs at 4T1 tumor sites (150 μL, 500 μM, 980 nm, 1150 nm long pass filter, exposure time: 300 ms). Scale bar: 10 μm.

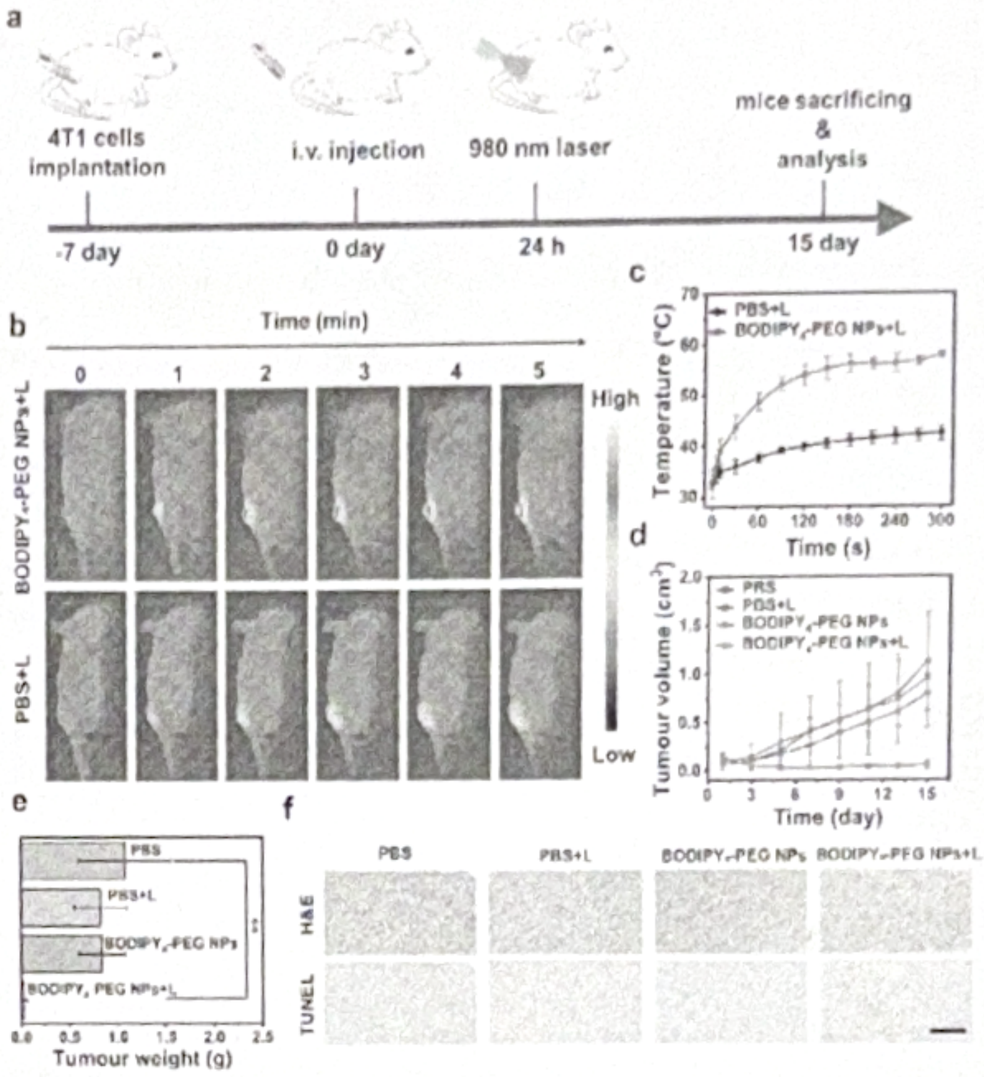

Fig. 5 *In vivo* antitumor efficacy of $BODIPY_4$–PEG NPs. (a) Schematic diagram of PTT using $BODIPY_4$–PEG NPs with 4T1 tumor-bearing mice. (b) Photothermal images of 4T1 tumor-bearing mice after the injection of PBS or $BODIPY_4$–PEG NPs under 980 nm laser light irradiation (1.00 W cm^{-2}, 5 min). (c) Temperature elevation at tumor sites under different treatments at various time points. (d) Tumor volume variation of mice in different treatment groups. (e) Average tumor weights of mice in different groups after 14 d of treatment. (f) H&E and TUNEL staining images of tumors. Scale bar: 200 μm. Data are presented as mean ± SEM (n = 5 per group), where n represents the number of independent experiments. $^{**}p < 0.01$.

the passive accumulation of $BODIPY_4$–PEG NPs at the tumor site through the enhanced permeability and retention (EPR) effect (Fig. 4f). As shown in Fig. S8 (ESI†), the fluorescence intensity of the tumor gradually increased over time, and the fluorescence ratio of the tumors to the surrounding normal tissues (T/NT) reached a peak of 6.30 at 24 h post-injection. In addition, the fluorescence distribution of $BODIPY_4$–PEG NPs in major organs and tumors at 48 h post-injection is exhibited in Fig. S9 (ESI†), with the signals primarily concentrated in the liver, spleen and tumor of the mouse.

In vivo imaging-guided PTT

Motivated by the outstanding antitumor ability of $BODIPY_4$–PEG NPs under 980 nm laser light irradiation *in vitro*, a 4T1 subcutaneous tumor model was established to evaluate its *in vivo* PTT performance. The 4T1 tumor-bearing mice were randomly divided into four treatment groups: PBS, PBS + L, $BODIPY_4$–PEG NPs, and $BODIPY_4$–PEG NPs + L, and then, as the fluorescence intensity at the tumor site reached the maximum value at 24 h after injection, a 980 nm laser (1.00 W cm^{-2}) was used to irradiate the tumor site for 5 min, while tumor temperatures were monitored in real-time using a thermal infrared imaging camera (Fig. 5a and b). The surface temperature of tumor sites in the $BODIPY_4$–PEG NPs + L group rapidly increased to 57.8 °C upon laser irradiation, whereas the tumor temperature in the PBS + L group rose by only about 9 °C from the baseline (Fig. 5c). In this experiment, despite the tumor temperature exceeding 50 °C, no obvious skin damage was observed. This is mainly attributed to the ability of NIR-II photothermal therapy to precisely target tumors while minimizing thermal damage to surrounding normal tissues. Over the next 14 d, tumor volume was measured every 2 d. Negligible tumor inhibition was observed in the PBS, PBS + L and $BODIPY_4$–PEG NPs groups, while marked tumor ablation occurred in the $BODIPY_4$–PEG NPs + L group. The tumor inhibition rate curves are provided in the ESI† (Fig. S11). The data indicate that the tumor suppression rate in the NIR-II PTT treatment group was significantly higher than that in the control group, thereby demonstrating a favorable anti-tumor effect. Notably, the tumor suppression rate in the NIR-II PT group reached 97.3% after 14 days, which was markedly superior to that of other treatment methods. The average tumor weight in various groups after 14 d of treatment showed a similar trend (Fig. 5e and Fig. S10, ESI†), indicating that the NIR-II imaging-guided PTT of $BODIPY_4$–PEG NPs achieved optimal antitumor efficacy. Notably, there were no significant changes in mouse body weight across the four groups throughout the treatment period (Fig. S12, ESI†). Furthermore, no obvious physiological or morphological irregularities were observed in the major organs (heart, liver, spleen, lungs and kidneys) across all groups (Fig. S13, ESI†). Moreover, the H&E and TUNEL staining of tumor tissues revealed more

extensive tumor damage in the $BODIPY_4$–PEG NPs + L group, demonstrating the superior PTT efficacy of $BODIPY_4$–PEG NPs *in vivo*. In addition, we provide the results of Caspase-3 and TUNEL immunofluorescence staining in the ESI† (Fig. S14). These results further confirm that the treatment regimen has a good effect on inducing cell apoptosis through photothermal therapy.

Experimental

Reagents and instruments

The organic reagents and biological reagents required for the experiment were purchased through commercial channels, and if there was no special explanation, they were directly used without secondary purification. Calcein-AM and propidium iodide (PI) were purchased from Beyotime (Shanghai, China). FBS, 0.25% Trypsin-EDTA, culture dishes, and 96-well culture plates were purchased from Gibco (Thermo Fisher Scientific, Waltham, MA, USA). CCK-8 and phosphate buffered saline (PBS) were purchased from Meilunbio® (Dalian, China).

The ^{1}H NMR spectra were recorded on a Bruker 400 MHz spectrometer in $CDCl_3$. Matrix-assisted laser desorption/ionization-time of flight mass spectrometry (MALDI-TOF-MS) was performed on a Bruker Autoflex Max. UV-vis-NIR absorption spectroscopy was recorded on a SHIMADZU UV-2600 spectrophotometer. Fluorescence emission spectroscopy was recorded on the iHR320-imaging-spectrometer. Dynamic light scattering (DLS) was performed on the Laser Particle Size and Zeta Potential Analyzer (Nano-ZS90, Malvern Corporation). TEM images were obtained on a JEOL JEM-2100 electron microscope (accelerating voltage: 120 kV).

DLS and TEM of $BODIPY_4$–PEG NPs

The particle size distribution of $BODIPY_4$–PEG NPs was measured by DLS at room temperature (25 °C). The aqueous solution of $BODIPY_4$–PEG NPs was dropped on a 300-mesh copper mesh, and the morphologies of the sample were observed with the TEM after natural drying.

Photothermal performances of $BODIPY_4$–PEG NPs

Aqueous solutions of $BODIPY_4$–PEG NPs at different concentrations (25, 50, 100, 200 μM) were placed in EP tubes and irradiated with an 808 nm, 980 nm, and 1064 nm laser at 1.00 W cm^{-2} for 5 min, separately. Pure water was used as the control group. After 5 min of irradiation, turn off the laser and wait for the aqueous solutions to drop to room temperature. A thermal infrared camera was used to detect the whole heating and cooling process and recorded the temperature every 15 s. The heating curves of $BODIPY_4$–PEG NP aqueous solutions (100 μM) with different power densities (0.25, 0.50, 0.75, 1.00 W cm^{-2}) were also recorded for 5 min irradiation. To evaluate the photothermal stability of the nanoparticles, the nanoparticle aqueous solutions were irradiated at a power density of 1.00 W cm^{-2} for 5 min, and then the laser was removed. After the temperature was reduced to room temperature, it was irradiated again for 5 min. This operation was repeated for 5 cycles, and each heating and cooling process was recorded with a thermal infrared camera. According to the previous report,[40] the PCE was calculated using the following formula:

$$\eta = \frac{hS\Delta T_{max} - Q_0}{I(1 - 10^{-A_{980}})} \quad (1)$$

where h is the heat transfer coefficient, S is the surface area of the container, and ΔT_{max} is the difference between the maximum temperature reached during the experiment and the initial room temperature. Q_0 is the heat dissipated from light absorbed by the sample cell itself. I is the incident laser power, and A_{980} is the absorbance of $BODIPY_4$–PEG NPs at 980 nm.

$$\theta = \frac{T - T_{min}}{T_{max} - T_{min}} \quad (2)$$

$$t = -\tau_s \ln(\theta) \quad (3)$$

$$\tau_s = \frac{m_0 C_0}{hs} \quad (4)$$

where τ_s is the sample system time constant, m_0 and C_0 are the mass and heat capacity of deionized water used as a solvent, respectively, and θ is the dimensionless parameter.

Cell culture

4T1 breast cancer cells and 3T3 cells were incubated in DMEM medium containing 10% fetal bovine serum (FBS) and 1% antibiotics (penicillin–streptomycin) and cultured in an incubator containing 5% CO_2 at 37 °C.

Cell uptake

4T1 cells (5×10^3 cells per well) and 3T3 cells (1×10^4 cells per well) were plated on 96-well plates and cultured in an incubator at 37 °C for 12 h. Different concentrations of $BODIPY_4$–PEG NPs (0, 25, 50, 75, 100 μM, 100 μL) were then added and *co*-cultured with cells for 12 h and 24 h, respectively. After co-incubation, the medium was removed and washed twice with PBS. Then, the cells were lysed and transferred to an EP tube. The fluorescence intensity of the cell lysates was recorded with a NIR-II camera. 4T1 cells were *co*-incubated with $BODIPY_4$–PEG NPs in 6-well plates for 24 h and then fixed with paraformaldehyde solution for 15 min, and photographed under a camera.

Cytotoxicity assay of $BODIPY_4$–PEG NPs

(1) Dark toxicity. 4T1 cells were seeded into 96-well plates at a density of 1×10^4 cells per well (100 μL total volume per well) and cultured in an incubator at 37 °C for 12 h. Then, the cells were *co*-incubated with $BODIPY_4$–PEG NPs at different concentrations (0, 25, 50, 75, and 100 μM) for 24 h. After incubation, CCK-8 was used to test the cell viability. CCK-8 (10 μL) was added to each well. After incubation for 4 h, the absorbance (450 nm) was measured by using a microplate reader.

(2) Phototoxicity. 4T1 cells were seeded into 96-well plates at a density of 1×10^4 cells per well and cultured in 5% CO_2 at 37 °C for 12 h. Then, $BODIPY_4$–PEG NPs at different concentrations (0, 12.5, 25, 35, 50, 75, 100 μM) were added into each well and incubated for another 12 h. The cells were irradiated with a

980 nm laser (1.00 W cm^{-2}) for 5 min. After irradiation, the 96-well plates were placed in an incubator again for 12 h. CCK-8 was used to test cell viability.

Live/dead cell staining

At a density of 4×10^4 cells per well, 4T1 cells were seeded in a 12-well plate. After incubation for 12 h, the cells were divided into PBS, PBS + L, $BODIPY_4$–PEG NPs, and $BODIPY_4$–PEG NPs + L groups, and 1 mL sample (50 μM) was added to each well for 12 h. Then, the cells were irradiated with a 980 nm laser for 5 min at a power density of 1.00 W cm^{-2} and rinsed twice with PBS. Subsequently, the cells were stained with a mixture of Calcein-AM (2 μM) and propidium iodide (PI, 8 μM) for 45 min, and imaged under a fluorescence microscope.

Establishment of 4T1 tumor model mice

The mice used in the experiment were purchased after approval by the Shanghai Experimental Animal Center. All animal experiments were conducted following the Animal Protection and Use Committee (IACUC) guidelines of the Shanghai Institute of Pharmaceutical Research, Chinese Academy of Sciences. Female Balb/c mice aged 6–8 weeks were used to establish 4T1 tumor models by subcutaneous or *in situ* injection of 50 μL 4T1 cell suspension (5×10^5 cells).

In vivo NIR-II fluorescence imaging

Before animal imaging, hair removal cream was used to remove hair from the whole mice's body. During the animal experiment, mice were anesthetized with isoflurane mixed liquid gas (3% isoflurane, 2 L min^{-1} O_2). $BODIPY_4$–PEG NPs were injected subcutaneously or intravenously into mice for imaging.

In vivo photothermal therapy

When the tumor volume reached approximately 70–100 mm^3, the tumor-bearing Balb/c mice were randomly divided into four groups (n = 5 per group): (1) PBS group, (2) PBS + L group, (3) $BODIPY_4$–PEG NPs group, (4) $BODIPY_4$–PEG NPs + L group. After 24 h of intravenous administration (500 μM, 150 μL) on the first day, mice in the laser irradiation groups (PBS + L group and $BODIPY_4$–PEG NPs + L group) were irradiated with a 980 nm laser (1.00 W cm^{-2}) for 5 min. The temperature changes at the tumor sites were recorded by a thermal infrared camera. The body weight and tumor size of the mice were monitored and recorded every other d within 14 d after treatment. After 14 d, the mice were sacrificed, the tumors and other major organs were stripped, and the tumors were weighed. The tumors and major organs were stored in 4% paraformaldehyde solution for hematoxylin and eosin (H&E) staining and TUNEL staining.

Statistical analysis

Statistical analysis was performed using the Origin Pro 2018C version. Data were expressed as the means ± SD. Differences were evaluated, and only those meeting the significance threshold were considered significant. No significant differences (ns) were observed unless $P < 0.05$ ($^*P < 0.05$, $^{**}P < 0.01$, $^{***}P < 0.001$ unless otherwise indicated).

Ethics approval statement

All animal experiments followed the protocols approved by the Institutional Animal Care and Use Committee at the Institute of Shanghai Immunology, School of Medicine, Shanghai Jiao Tong University (A-2022-031).

Conclusions

In summary, water-soluble $BODIPY_4$–PEG NPs effectively meet the demands of a large conjugated system for NIR-II fluorescence while improving water solubility for enhanced fluence emission performance and biostability. The red-shifted emission of $BODIPY_4$–PEG NPs enables attractive NIR-II fluorescence imaging, allowing for clear distinction of blood vessels and lymph nodes from surrounding tissues. In addition, through its passive targeting ability, $BODIPY_4$–PEG NPs accumulated at the tumor site, achieving precise and efficient PTT guided by the sensitive NIR-II fluorescence imaging, with a maximum T/NT ratio of 6.30. Overall, these PEGylated BODIPY nanoparticles demonstrate significant potential in NIR-II imaging-guided cancer management.

Author contributions

Yuan Wang: conceptualization, data curation, formal analysis, investigation, methodology, visualization, writing – original draft. Tongtong Shan: methodology, software, validation, writing – review & editing. Jiahao Zheng: supervision, writing – review & editing. Jia Tian: supervision, writing – review & editing. Weian Zhang: funding acquisition, project administration, resources, supervision, writing – review & editing.

Data availability

The authors declare that the data can be obtained from the corresponding author on request.

Conflicts of interest

The authors declare no competing interests.

Acknowledgements

This work was financially supported by the National Natural Science Foundation of China (52333014), and the Science and Technology Commission of Shanghai Municipality (22142201100 and 24520713200).

Notes and references

1 H.-B. Cheng, X. Cao, S. Zhang, K. Zhang, Y. Cheng, J. Wang, J. Zhao, L. Zhou, X.-J. Liang and J. Yoon, *Adv. Mater.*, 2022, **35**, 2207546.

2 S. He, J. Song, J. Qu and Z. Cheng, *Chem. Soc. Rev.*, 2018, **47**, 4258–4278.
3 W. Feng, Y. Lv, Z. Chen, F. Wang, Y. Wang, Y. Pei, W. Jin, C. Shi, Y. Wang, Y. Qu, W. Ji, L. Pu, X.-W. Liu and Z. Pei, *Chem. Eng. J.*, 2021, **417**, 129178.
4 Y. Zhang, H. Tao, Q. Li, W. Sheng, Y. Xu, E. Hao, M. Chen, Z. Liu and L. Feng, *J. Controlled Release*, 2020, **326**, 256–264.
5 H. Dai, X. Wang, J. Shao, W. Wang, X. Mou and X. Dong, *Small*, 2021, **17**, 2102646.
6 K. Song, X. Su, W. Zhao, F. Ai, A. Umar and S. Baskoutas, *Chem. Eng. J.*, 2024, **485**, 150067.
7 Y. Wan, W. Chen, Y. Liu, K.-W. Lee, Y. Gao, D. Zhang, Y. Li, Z. Huang, J. Luo, C.-S. Lee and S. Li, *Adv. Mater.*, 2024, **36**, 2405966.
8 T. Zhang, C. Ma, T. Sun and Z. Xie, *Coord. Chem. Rev.*, 2019, **390**, 76–85.
9 X. Ding, C. H. Liow, M. Zhang, R. Huang, C. Li, H. Shen, M. Liu, Y. Zou, N. Gao, Z. Zhang, Y. Li, Q. Wang, S. Li and J. Jiang, *J. Am. Chem. Soc.*, 2014, **136**, 15684–15693.
10 Q. Zheng, X. Liu, Y. Zheng, K. W. K. Yeung, Z. Cui, Y. Liang, Z. Li, S. Zhu, X. Wang and S. Wu, *Chem. Soc. Rev.*, 2021, **50**, 5086–5125.
11 Q. Miao and K. Pu, *Adv. Mater.*, 2018, **30**, 201801778.
12 G. Hong, A. L. Antaris and H. Dai, *Nat. Biomed. Eng.*, 2017, **1**, 0010.
13 Y. Liu, L. Teng, H.-W. Liu, C. Xu, H. Guo, L. Yuan, X.-B. Zhang and W. Tan, *Sci. China: Chem.*, 2019, **62**, 1275–1285.
14 H. Yueyang, L. Jinyan, B. Jingwen, S. Xiao, L. Kangliang, Z. Yuanyuan, Q. Zishan, C. Weiling, L. Yang, L. Xiaolong and Z. Guojun, *Adv. Sci.*, 2025, **12**, 2413385.
15 P. Ananthi, V. Naveen Raj, K. Hemkumar, A. Praveen and P. Anitha, *ACS Sustainable Chem. Eng.*, 2025, **14**, 4c06496.
16 V.-N. Nguyen, H. L. Pham and X. T. Nguyen, *Dyes Pigm.*, 2024, **230**, 112359.
17 P. Chinna Ayya Swamy, G. Sivaraman, R. N. Priyanka, S. O. Raja, K. Ponnuvel, J. Shanmugpriya and A. Gulyani, *Coord. Chem. Rev.*, 2020, **411**, 213233.
18 D. Xi, M. Xiao, J. Cao, L. Zhao, N. Xu, S. Long, J. Fan, K. Shao, W. Sun, X. Yan and X. Peng, *Adv. Mater.*, 2020, **32**, 1907855.
19 Z. Tao, G. Hong, C. Shinji, C. Chen, S. Diao, A. L. Antaris, B. Zhang, Y. Zou and H. Dai, *Angew. Chem., Int. Ed.*, 2013, **52**, 13002–13006.
20 L. Chen, D. Chen, Y. Jiang, J. Zhang, J. Yu, C. C. DuFort, S. R. Hingorani, X. Zhang, C. Wu and D. T. Chiu, *Angew. Chem., Int. Ed.*, 2019, **58**, 7008–7012.
21 Q. Zhang, P. Yu, Y. Fan, C. Sun, H. He, X. Liu, L. Lu, M. Zhao, H. Zhang and F. Zhang, *Angew. Chem., Int. Ed.*, 2020, **60**, 3967–3973.
22 X. Cai, A. Bandla, C. K. Chuan, G. Magarajah, L.-D. Liao, D. B. L. Teh, B. K. Kennedy, N. V. Thakor and B. Liu, *Mater. Horiz.*, 2018, **6**, 311–317.
23 H. Zhao, Y. Wang, Q. Chen, Y. Liu, Y. Gao, K. Müllen, S. Li and A. Narita, *Adv. Sci.*, 2024, **11**, 2309131.
24 Y.-W. Tai, Y.-C. Chiu, P.-T. Wu, J. Yu, Y.-C. Chin, S.-P. Wu, Y.-C. Chuang, H.-C. Hsieh, P.-S. Lai, H.-P. Yu and M.-Y. Liao, *ACS Appl. Mater. Interfaces*, 2018, **10**, 5161–5174.
25 Q. Wu, Y. Zhu, X. Fang, X. Hao, L. Jiao, E. Hao and W. Zhang, *ACS Appl. Mater. Interfaces*, 2020, **12**, 47208–47219.
26 Q. Wu, Z. Kang, Q. Gong, X. Guo, H. Wang, D. Wang, L. Jiao and E. Hao, *Org. Lett.*, 2020, **22**, 7513–7517.
27 W. Shao, Q. Wei, S. Wang, F. Li, J. Wu, J. Ren, F. Cao, H. Liao, J. Gao, M. Zhou and D. Ling, *Mater. Horiz.*, 2020, **7**, 1379–1386.
28 Z. Yushi, Y. Xuya, L. Lingpeng, X. Yigang, Z. Hanjie, M. Zhuo, Z. Yuqin, Y. Cuihong, W. Lu, Z. Pengcheng, L. Sitong, O. Meitong, L. Ran, Z. Dunwan, L. Wen and M. Lin, *J. Fluoresc.*, 2024, **33**, 297–304.
29 Z. Yushi, Y. Xuya, L. Lingpeng, X. Yigang, Z. Hanjie, M. Zhuo, Z. Yuqin, Y. Cuihong, W. Lu, Z. Pengcheng, L. Sitong, O. Meitong, L. Ran, Z. Dunwan, L. Wen and M. Lin, *J. Controlled Release*, 2024, **376**, 1115–1129.
30 C. Zhou, Z. Li, Z. Zhu, G. W. N. Chia, A. Mikhailovsky, R. J. Vázquez, S. J. W. Chan, K. Li, B. Liu and G. C. Bazan, *Adv. Mater.*, 2022, **34**, 2201989.
31 K. Li, X. Duan, Z. Jiang, D. Ding, Y. Chen, G.-Q. Zhang and Z. Liu, *Nat. Commun.*, 2021, **12**, 2376.
32 I. W. Badon, J. Lee, T. Pegarro Vales, B. K. Cho and H.-J. Kim, *J. Photochem. Photobiol., A*, 2019, **377**, 214–219.
33 A. M. Saad, S. Nadi, F. Ibraheem, Y. A. Badr, I. A. Mahdy, Z. M. Abd El-Fattah and A. El-Sayed, *Opt. Mater.*, 2024, **147**, 0925–3467.
34 Q. Yang, Z. Hu, S. Zhu, R. Ma, H. Ma, Z. Ma, H. Wan, T. Zhu, Z. Jiang, W. Liu, L. Jiao, H. Sun, Y. Liang and H. Dai, *J. Am. Chem. Soc.*, 2018, **140**, 1715–1724.
35 M. Su, Q. Han, X. Yan, Y. Liu, P. Luo, W. Zhai, Q. Zhang, L. Li and C. Li, *ACS Nano*, 2021, **15**, 5032–5042.
36 D. An, J. Fu, B. Zhang, N. Xie, G. Nie, H. Ågren, M. Qiu and H. Zhang, *Adv. Funct. Mater.*, 2021, **31**, 2101625.
37 Y. Song, M. Lu, Y. Xie, G. Sun, J. Chen, H. Zhang, X. Liu, F. Zhang and L. Sun, *Adv. Funct. Mater.*, 2022, **32**, 2206802.
38 S. Bian, X. Zheng, W. Liu, Z. Gao, Y. Wan, J. Li, H. Ren, W. Zhang, C.-S. Lee and P. Wang, *Biomaterials*, 2023, **303**, 122380.
39 D. W. Siemann, D. J. Chaplin and M. R. Horsman, *Cancer Invest.*, 2017, **35**, 519–534.
40 D. K. Roper, W. Ahn and M. Hoepfner, *J. Phys. Chem. C*, 2007, **9**, 3636–3641.